Magnetotransport Measurements of InAlGaAs/AlGaAs Heterostructures for Optimizing Photocathode Material Quality

Amelia Schaeffer
2022 Physics REU, Department of Physics, University of California Santa Barbara, Santa Barbara, California 93106, USA and Department of Physics, Reed College, Portland, Oregon 97202, USA

Faculty Advisor: Dr. Christopher Palmstrøm
Department of Materials, University of California Santa Barbara, Santa Barbara, California 93106, USA and Department of Electrical and Computer Engineering, University of California Santa Barbara, Santa Barbara, California 93106, USA

Graduate Advisors: Jason Dong and Aaron Engel
Department of Materials, University of California Santa Barbara, Santa Barbara, California 93106, USA
(Dated: September 12, 2022)

GaAsP/GaAs photocathodes currently in use for spin-polarized electron beams at particle accelerators are not commercially available, easy to make, or well-suited for further innovation. In this work, we study a photocathode candidate system of 10 quantum wells formed by alternately growing InAlGaAs and AlGaAs on a relatively inexpensive, commercially available GaAs (001) wafer via molecular beam epitaxy. We optimize material quality of this system by comparing magnetotransport-derived mobilities for samples grown with variations in growth temperature and AlGaAs barrier construction. From Hall measurements and analysis of Shubnikov-de Haas oscillations, we determine electron sheet carrier density (n_s), transport mobility (μ_t), transport lifetime (τ_t), effective mass (m^*), quantum mobility (μ_q), and quantum lifetime (τ_q) in each sample. We did not find that any of the modifications to the AlGaAs barriers improved transport mobility but that cooler growth temperatures, and higher growth temperatures to a lesser extent, led to notably better transport mobilites, indicating cooler growth is favorable for producing the highest quality material in this system.

I. INTRODUCTION

Electron beams are of great utility in particle accelerators for probing the structure of nucleons, characterizing quark confinement, and cooling other beams of particles, such as protons or positrons [1]. In recent years, there has been increasing demand for the advancement of spin-polarized electron beam sources in order to test parity violations of the standard model and many other strong and electro-weak interactions [2, 3]. One of the main barriers to such advancement is the improvement of the photocathodes from which spin-polarized electron beams are produced. The GaAsP-based photocathodes currently in use are difficult to grow, not reliably commercially available, and have little room for innovation in the material system design.

In order to understand how we can develop the next generation of spin-polarized photocathodes, it is valuable to consider the physics behind producing a spin-polarized electron beam. All of these photocathodes are based on GaAs and exploit its interaction with circularly polarized light. Due to quantum mechanical selection rules, when circularly polarized light is incident on GaAs, it excites electrons from the heavy hole valence band to one spin state of the conduction band and electrons from the light hole valence band to the opposite spin state of the conduction band, with heavy hole electrons being promoted three times as often [1]. Which conduction band spin state these electrons will be promoted into is determined by the chirality of the incident light. In bulk GaAs, this leads to a maximum spin polarization of 50%. This value can be increased by introducing mechanical strain into the crystal to energetically separate the heavy hole and light hole bands. Doing so changes the energy gaps between these two valence band states and the conduction band states by different amounts. Additionally, quantum confinement of the charge carriers will also contribute to breaking the heavy hole/light hole degeneracy. Through these two effects, this will theoretically enable targeted excitation from a single valence band state and 100% spin-polarized photoemission. While there are many complications to physically realizing such a polarization, increasing polarization as high as possible while maintaining good quantum efficiency is a major aim of designing a spin-polarized photocathode.

One of the main challenges in designing photocathodes based on strained GaAs is that past the critical thickness the crystal structure will relax and it will lose its enhanced spin polarization. One approach that circumvents this issue is to use strained superlattices, or materials in which two or more semiconductors are layered in a repeating fashion. These materials are specifically designed so that the adjacent layers will have lattice constant mismatches of up to a few percent to introduce mechanical strain and layers under the critical thickness [4]. When compared to a single layer of a strained GaAs, whose thickness is limited to avoid relaxation, these structures allow for a sample with a larger total amount of a strained

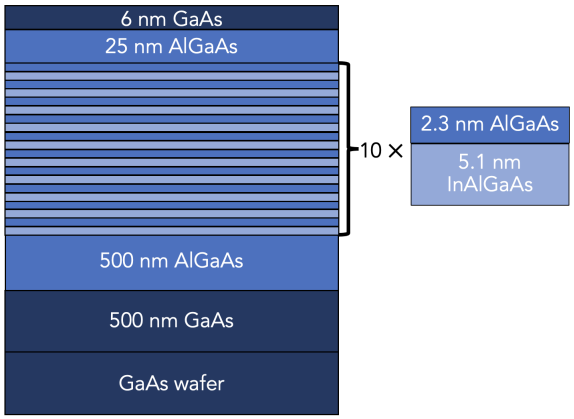

FIG. 1. Schematic of the basic design of the photocathodes we study in this work. For the InAlGaAs wells, the default Al content is 23% and for the AlGaAs barriers it is 27.4%. See Tab. I for composition details for individual samples.

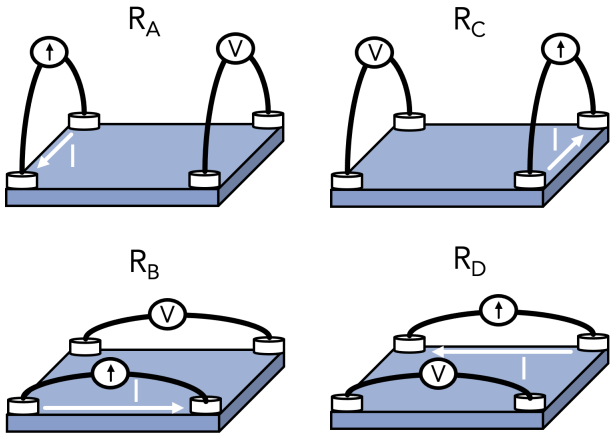

FIG. 2. Schematic of how longitudinal resistance measurements are performed on samples to aid in correcting for sample and contact asymmetries using R_A, R_B, R_C, and R_D. The discrepancy in side lengths on a sample is exaggerated in this figure to demonstrate the technique.

GaAs to act as the active part of the photocathode.

Additionally, these strained superlattices can be used to build systems of multiple quantum wells by alternating semiconductors of different band gaps. This effectively confines charge carriers to in-plane motion and creates a 2-D electron gas (2DEG) transport system. Since electron energies are confined to discrete steps in this 2DEG transport, for a laser emitting light of the right energy, each photon has a higher probability of resulting in a photoemission by the material, thus increasing the quantum efficiency.

Advances in GaAs-based spin-polarized photocathodes utilizing strained superlattices with varying levels of Al and In incorporated into the GaAs structure have reported some of the highest spin-polarization values realized in photocathode materials [5]. In this work, we use magnetotransport measurements to quantify charge carrier properties (density, transport and quantum mobilities, transport and quantum lifetimes, and effective mass) of InAlGaAs/AlGaAs multiple quantum well systems of varied growth temperatures and composition to determine which conditions optimize material quality for photocathode development.

II. EXPERIMENT

All samples studied are n-type heterostructures grown on commercially available (001) GaAs wafers via molecular beam epitaxy. Modulation doping layers of Si are included in the AlGaAs barriers with 2.3 Å between the dopants and each quantum well. A schematic of the control sample structure is shown in Fig. 1 and specific sample details are given in Tab. I (bold text highlights the parameter varied in that sample). Ohmic contacts to the four corners of the approximately square samples are made with InSn that is annealed at 375°C for two hours in order to allow InSn diffusion down to the quantum well region. Gold wires are used to connect the sample to a Quantum Design Physical Property Measurement System (PPMS) capable of generating fields up to 14 T and cooling to liquid helium temperatures. The PPMS output is connected to lock-in amplifiers (Stanford Research Systems SR830) from which readouts are recorded. Initial zero-field measurements of longitudinal and transverse resistances are taken to ensure there is not large sample asymmetry present.

For each sample, four longitudinal resistance measurements (R_A, R_B, R_C, and R_D) are taken in four orientations where the set of probes is rotated 90° relative to the sample between each measurement. Hall resistances were measured for two orientations on the sample, offset by a 90° rotation. A schematic of this is shown in Fig. 2.

III. RESULTS

A. Sheet Carrier Density and Transport Mobility

From the raw data, we anti-symmetrize all Hall resistance measurements and symmetrize all longitudinal measurements in order to reduce the effects of signal intermixing in the samples. Intermixing occurs when there are slight asymmetries or misalignments between the contacts so that they are slightly offset in both the Hall and longitudinal directions. This means that some small amount of the "unintended" mode of transport (i.e. Hall transport for a longitudinal measurement and vice versa) will be present in the measured signal and will need to be removed to obtain accurate data about the primary resistance being measured. Examples of this data can be seen in Fig. 3 for sample 2. Since measurements along the same path with current flowing in opposite directions

TABLE I. Sample Growth Temperatures and Compositions

Sample	Growth Temperature (°C)	Alloy Type	% Al in Well	% Al in Barrier	Barrier Thickness (nm)	Number of Wells
1	520	Analog	23	27.4	2.3	10
2	**505**	Analog	23	27.4	2.3	10
3	**535**	Analog	23	27.4	2.3	10
4	520	Analog	**26**	**30.4**	2.3	10
5	520	**Digital**	23	27.4	2.3	10
6	520	**Digital**	23	**40.0**	2.3	10
7	520	Analog	23	27.4	**3.0**	10
8	520	Analog	23	27.4	2.3	**6**

TABLE II. Values Calculated From Magnetotransport Data

Sample	n_s (10^{12}cm^{-2})	μ_t (cm^2/V·s)	μ_q (cm^2/V·s)	τ_t (10^{-14}s)	τ_q (10^{-14}s)	τ_t/τ_q	m^*/m_e[a]
1	4.65	417	1176	2.1	5.9	0.35	0.0882(23)
2	2.84	649	1418	3.2	7.0	0.46	0.087(4)
3	4.45	536	865	2.6	4.3	0.62	0.087(5)
4	2.12	408	2088	2.3	12.0	0.20	0.100(13)
5	1.54	213	1459	1.4	9.6	0.15	0.116(13)
6[b]	-	-	-	-	-	-	-
7	9.17	387	1036	1.9	5.0	0.37	0.0805(4)
8	1.89	166	1128	0.9	5.9	0.15	0.091(6)

[a] Many effective masses show magnetic field dependence and values are reported around $B = 10$ T.
[b] Unable to be measured due to Schottky-like behavior at low temperatures, likely due to carrier-depleted quantum wells.

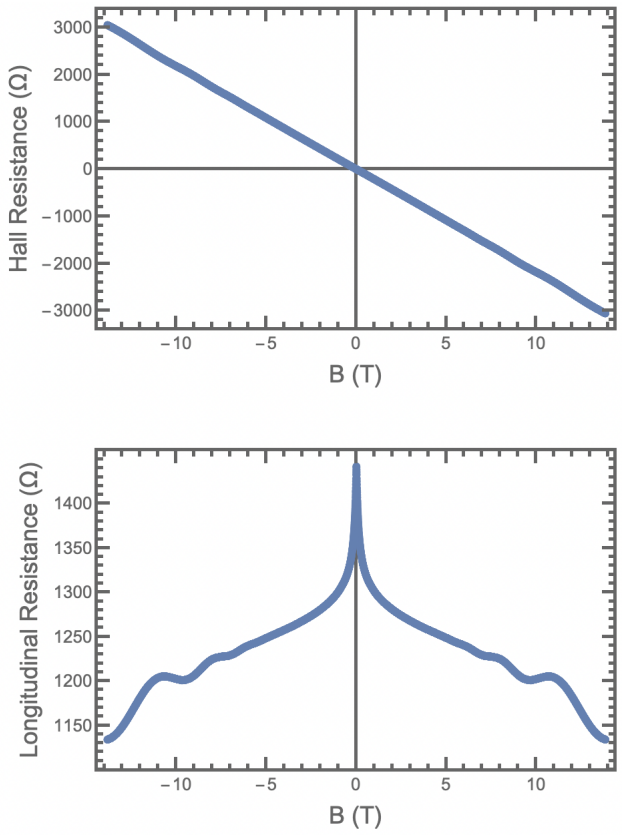

FIG. 3. Anti-symmetrized Hall resistance and symmetrized longitudinal resistance as a function of applied magnetic field for sample 2.

(R_A and R_C or R_B and R_D) should theoretically be the same, we average these values to help correct for the effects of any contact or sample asymmetry present in the measurement:

$$R_1 = \frac{R_A + R_C}{2} \tag{1a}$$

$$R_2 = \frac{R_B + R_B}{2}. \tag{1b}$$

These resistance values are related to the 2D sheet resistance of the sample, R_s, via the van der Pauw equation [6]:

$$\exp[-\pi R_A/R_s] + \exp[-\pi R_B/R_s] = 1. \tag{2}$$

With R_A and R_B calculated from measurements, we numerically solve Eq. (2) for R_s.

When we plot Hall resistance as a function of applied magnetic field for samples with a single type of charge carrier, we observe linear behavior with a slope of $\frac{1}{n_s e}$ where e is the elementary charge and n_s is the sheet charge carrier density. Thus, from the slope of these plots, we extract n_s and use it to calculate electron transport mobility, which is given by

$$\mu_t = \frac{1}{e n_s R_s}. \tag{3}$$

Tab. II contains all of the values calculated from analysis of the mangetotransport measurements where sheet carrier density (n_s), transport mobility (μ_t), quantum mobility (μ_q), transport lifetime (τ_t), and quantum lifetime (τ_q) are reported for $T = 2$ K.

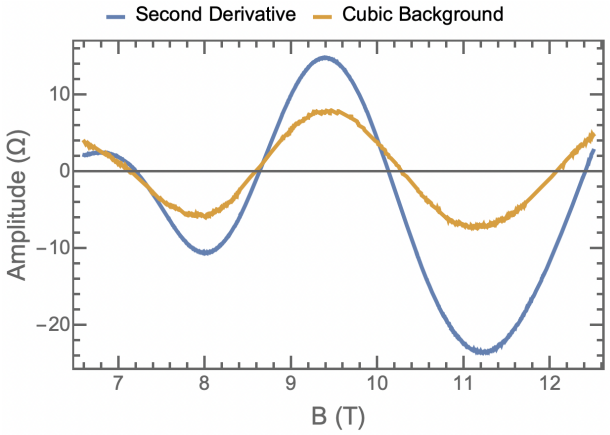

FIG. 4. Shubnikov-de Haas oscillations for sample 2 at 2 K as isolated via two different methods: in blue, the second derivative of the symmetrized R_{xx} signal, and in orange the residuals of subtracting a best-fit cubic polynomial over the magnetic field range shown.

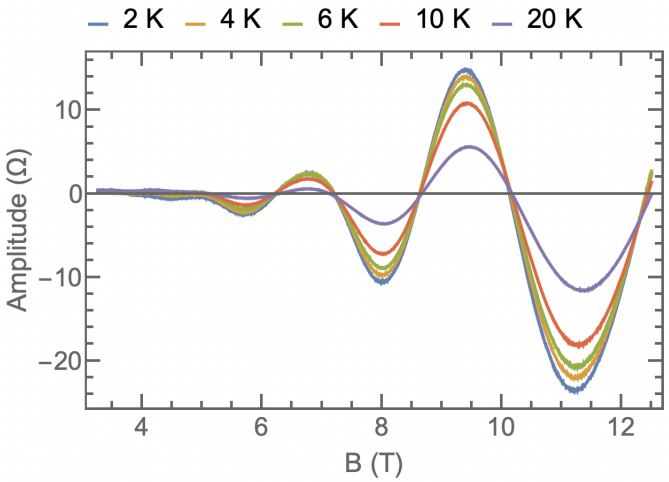

FIG. 5. Amplitude of Shubnikov-de Haas oscillations as a function of magnetic field for sample 2, shown for several temperatures. Oscillations were isolated by taking the second derivative of symmetrized R_{xx} data and adjusting the offset so that oscillations occured about zero.

All of the values of n_s measured at 2 K were between 10^{12} cm^{-2} and 10^{13}cm^{-2} with the most notable measurement being that of sample 6, which showed significantly higher charge carrier density than the other samples.

The highest transport mobility of $\mu_t = 648$ cm^2/V·s was observed in the sample grown at 505°C. Mobility decreased somewhat in the control sample grown at 520°C but increased again at 535°C. This may be due to In partial evaporation at 520°C but even more pronounced In evaporation at 535°C, as In re-evaporation has been previously observed in MBE growth of similar samples [7]. This could explain the changing mobilities because at 535°C, the wells approach AlGaAs more closely, thus decreasing disorder and increasing μ_t.

While even the highest electron mobilities reported here are about an order of magnitude below what would be considered decent electron mobility in many electronic applications, we were seeking to optimize within a design practical for real photocathode fabrication and use. Specifically, in our design, the dopant atoms are placed very close to the InAlGaAs wells to increase the efficiency of the dopant. However, this creates ionized atoms in close physical proximity to the wells, greatly increasing the frequency of electron scattering events. Within these limitations, it appears that the cooler growing temperature of 505°C optimizes μ_t.

B. Shubnikov-de Haas Oscillation Analysis

In order to extract further information about the charge carrier environment in the material, we turn to the analysis of the Shubnikov-de Haas oscillations that occur in the longitudinal resistance measurements at high magnetic fields. Under these conditions, the density of states distribution begins to develop peaks near quantized electron energies in a precursor to the Integer Quantum Hall Effect [8]. As these peaks move past the Fermi energy, this causes fluctuations in the number of states available to electrons at the Fermi energy, and therefore fluctuations in the longitudinal resistance of the material.

We tested two different methods to isolate the Shubnikov-de Haas (SdH) oscillations from the background signal. In the first method, we fit a cubic polynomial to the symmetrized data starting at the magnetic field at which the onset of visible SdH oscillations begin. (We found that cubic fits to the symmetrized signal starting at lower fields were worsened by the presence of pronounced weak localization and were therefore not pursued further.) We then plot the residuals from this fit as a function of magnetic field in order to get the polynomial background-subtracted oscillations. In the second method, we interpolate the symmetrized R_{xx} data, smooth it slightly, and differentiate it twice. While this is intended to isolate the oscillatory behavior of the original signal, these second derivatives do not oscillate around zero due to the curvature of the background signal. In order to compensate for this, we manually shift the signals to oscillate around zero. For each sample, we apply the same shift to all oscillatory curves of different temperatures. A comparison of the signal isolated by each method for one sample is shown in Fig. 4. In general, the second derivative method appears to be more reliable for isolating clear oscillatory signal where the amplitude of oscillation increases with increasing magnetic field magnitude. Thus, the values we report in this work are calculated from second derivative method.

Once we isolate the oscillations from the background signal, we expect them to be periodic with respect to $1/B$ where B is the magnetic field [8]. The amplitude of these

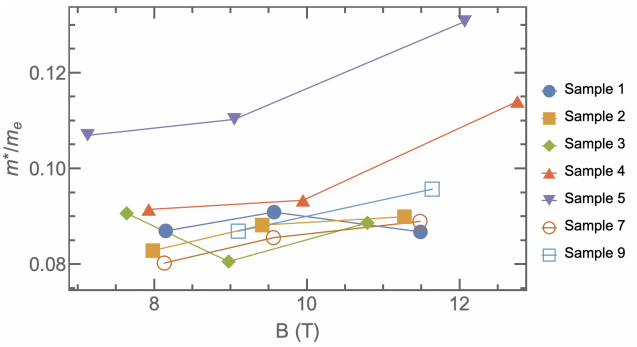

FIG. 6. Calculated effective mass as a function of the magnetic field of the Shubnikov-de Haas oscillation extrema from which it was calculated for all measured samples. Most samples studied showed an overall increase in calculated effective mass with increasing magnetic field.

oscillations is given by [9]

$$\Delta R_{xx} = 4R_0 \frac{\chi}{\sinh \chi} \exp[-\frac{\pi}{\omega_c \tau_q}] \tag{4}$$

where ΔR_{xx} is the oscillation amplitude, R_0 is the sheet resistance at $B = 0$, $\omega_c = \frac{eB}{m^*}$ is the cyclotron frequnecy, τ_q is the quantum lifetime, and χ is given by [9, 10]

$$\chi = \frac{2\pi^2 k_B T}{\Delta E}. \tag{5}$$

In this equation, ΔE is the Landau level energy gap which can be written as

$$\Delta E = \hbar\omega_c = \frac{\hbar e B}{m^*}. \tag{6}$$

The oscillatory signal isolation is repeated for every temperature at which the samples were measured; samples 1 and 2 were measured at 2 K, 4 K, 6 K, 10 K, and 20 K and the rest of the samples were measured at 2 K, 4 K, 10 K, 15 K, and 20 K. The isolated SdH oscillations at different temperatures in sample 2 are shown in Fig. 5. For each temperature, we differentiate the amplitude vs. magnetic field curve (such as those shown in Fig. 5) and solve for the roots in order to find the field values for which local extrema were observed. For each sample, we average these field values across all temperatures measured for each oscillation. Then, we normalize the amplitudes of oscillation at those averaged field values using the amplitude of the lowest temperature measurement. From Eq. (4), we can express these normalized amplitudes as [9, 11]

$$\frac{\Delta R_{xx}(T,B)}{\Delta R_{xx}(T_0,B)} = \frac{T \sinh(2\pi^2 T_0 \frac{k_B}{\Delta E})}{T_0 \sinh(2\pi^2 T \frac{k_B}{\Delta E})}. \tag{7}$$

We then plot $\frac{\Delta R_{xx}(T,B)}{\Delta R_{xx}(T_0,B)}$ as a function of T, as shown in Fig. 7. The curve shown is the best fit curve of equation Eq. (7) when $T_0 = 2$ K and $\frac{k_B}{\Delta E}$ is taken as a fitting parameter. As has been noted in the literature, using m^* directly as a fitting parameter can give erroneous values [12]. We observe similar issues when attempting to fit directly to m^*, or even ΔE. We find that using $k_B/\Delta E$ as a fitting parameter and then converting the fit value back to ΔE, and to m^* using Eq. (6) circumvents this issue.

Most samples have three clear SdH oscillation extrema that we are able to analyze for effective mass calculations, but due to the weakness of the oscillations for sample 8, there are only two extrema that we can use in calculations. In most samples the calculated effective mass is higher when calculated from SdH oscillation extrema that occured at higher fields, as shown in Fig. 6. Interestingly, this effect of increasing effective mass with magnetic fields seems to be more pronounced in samples where modifications to the AlGaAs barrier were made (samples 2, 3, 4, 5, and 7) relative to the samples where only growth temperature was varied and the control design is used. The m^* values we report are averaged from the values calculated between fields of 8 and 13 T. We believe that accounting the magnetic-field dependence of effective mass would involve g-factor corrections beyond the scope of this work.

However, we can compare these to the effective mass values calculated for strained AlGaAs with 27.4% Al which is $m^* = 0.08398\ m_e$ and for strained InAlGaAs with 23% Al and 61% Ga, which is $m^* = 0.07778\ m_e$ (calculated from parameters in Ref. [13]). For all samples that we were able to measure, except for sample 7 in which we increased the barrier thickness, we see that our m^* values are notably higher than these predicted values. Several factors are likely at play here, including influences from the energy and physical confinement of electrons (due to band offsets and the ultrathin nature of the layers respectively), as well as specific factors within individual sample design. The most significant increase observed in the effective mass is due to the use of a digital alloy AlGaAs barrier, followed by the sample with a global 3% increase in Al content.

The average m^* values reported in Tab. II were used to calculate τ_t using

$$\tau_t = \frac{\mu_t m^*}{e}. \tag{8}$$

The values calculated follow nearly the same trend as μ_t, except for samples 1 and 4, where sample 1 has a slightly higher value of μ_t and sample 4 has a slightly higher value of τ_t.

For quantum lifetime (τ_q), we can see that [9, 14]

$$\ln(D) = \ln\left[\frac{\Delta R_{xx}(T,B)}{\Delta R_{xx}(T_0,B)} \frac{\sinh(\chi)}{\chi}\right] = C_0 - \frac{\pi m^*}{e\tau_q B} \tag{9}$$

where C_0 is a constant. If we plot $\ln(D)$ as a function of $1/B$ and perform a linear fit to this data, the slope is given by $-\frac{\pi m^*}{e\tau_q}$, from which we extract τ_q. Once we have

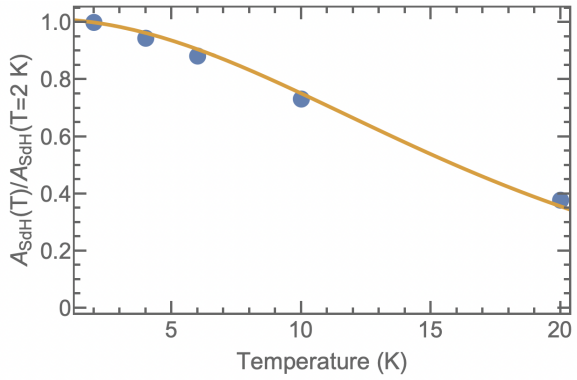

FIG. 7. Amplitudes of Shubnikov-de Haas oscillation at $B = 9.41$ T normalized to the amplitude at 2 K as a function of temperature for sample 2. The line is the best fit of Eq. (7) where $\frac{k_B}{\Delta E}$ is used as the fitting parameter.

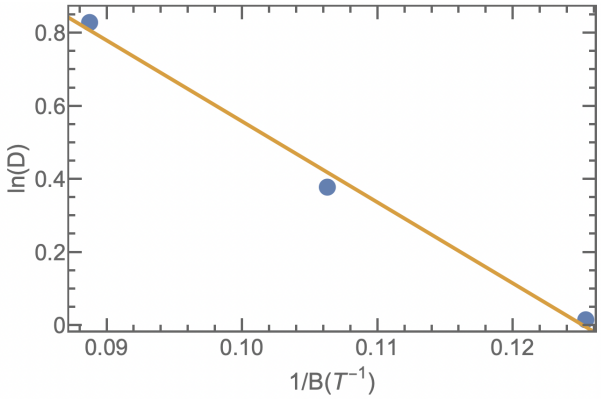

FIG. 8. Dingle plot used to calculate τ_q for sample 2 based on Eq. (9).

a value for τ_q, we calculate μ_q using

$$\mu_q = \frac{\tau_q e}{m^*} \tag{10}$$

the values of which are given in Tab. II. While none of the other samples outperformed sample 2 in transport mobility, sample 4, which had a 3% increase in aluminum across the AlGaAs barriers and InAlGaAs wells, showed only a small decrease in transport mobility and a large increase in quantum mobility and lifetime relative to the control sample. Interestingly, the quantum and transport mobilities do not track well together across the samples studied, but this may be due to the fact that the transport mobility is weighted by large angle scattering [9]. The small ratios of τ_t/τ_q across all samples, taken together with the fact that the Si modulation doping layers are placed very close to the InAlGaAs wells suggest that large-angle impurity scattering is the dominant scattering mechanism for electrons in all of the samples studied [15].

We also perform basic frequency analysis on the SdH oscillations. Since the oscillations are predicted to be periodic with respect to $1/B$, we plot the amplitudes as a function of $1/B$ and use a discrete Fourier transform to isolate the frequencies (B_F) of oscillation. The discrete Fourier transforms for all samples had low resolution at low frequencies due to how few complete periods of oscillation were able to be analyzed. In all samples only one frequency could visibly be identified, however, calculating the differences in the $1/B$ positions of extrema prior to passing the data through the discrete Fourier transform revealed that the period of oscillation was not constant and drifted longer for higher values of $1/B$ (lower magnetic fields). This may be due to two close frequencies present in the signal contributing to the changing period that are not able to be resolved in the discrete Fourier transform.

From these values of B_F shown in Tab. III, we calculate sheet carrier density as derived from the SdH oscillations, n_{SdH} to be [9]

$$n_{SdH} = \frac{geB_F}{h} = \frac{2eB_F}{h} \tag{11}$$

where g is the Landau level degeneracy which we take to be 2 for spin-unresolved Landau levels. By taking the ratio of n_s to n_{SdH}, we are able to see whether we are getting transport participation from multiple subbands in the quantum well structure. From the results in Tab. III, we can see that our values of n_s were consistently significantly larger than the corresponding n_{SdH} values. While the poor resolution of the discrete Fourier transform to calculate B_F limits the certainty of these results, this is a first indication that we may be seeing multiple subbands participating in this transport.

Lastly, we also attempt to calculate the Landau level index, N, for the minima observed in the SdH oscillations. When the Fermi level lies between two Landau levels, a minima is observed in R_{xx} electrical resistance as a precursor to the Integer Quantum Hall Effect in which this resistance drops to zero [8]. In order to calculate N we divide B_F for that sample by the field value at which a minima occurs in the 2 K SdH oscillations. The results of this division are shown in the last column of Tab. III where the magnetic field at which a minima appears, B, and the Landau level index calculated at that field value, N, are given as ordered pairs. Theoretically, these values should be integers. While some values are close to integer values, the majority of the values depart significantly from integers. We believe this to be due to inaccuracy in the B_F values due to the very low resolution of the discrete Fourier transform because of the low number of periods that appear in the raw data and can be used. In general, we see that this resolution places severe limitations on the reliability and precision of the values derived from this SdH frequency analysis presented in Tab. III.

As a general note on uncertainty in this work, we do not include statistical or systematic uncertainty in the values reported here, except in the case of m^* in Tab. II, as doing so is not standard to the discipline. We estimate that the largest sources of error introduced into

TABLE III. Values Calculated From Shubnikov-de Haas Frequency Analysis

Sample	B_F (T)	n_{SdH} (10^{12}cm^{-2})	n_s/n_{SdH}	(B, N)
1	25	1.21	3.8	(8.14, 3.07), (11.45, 2.19)
2	24.5	1.18	2.4	(7.97, 3.07), (11.23, 2.18)
3	24.5	1.18	3.8	(7.64, 3.21), (10.75, 2.28)
4	16.75	0.80	2.6	(7.90, 2.12), (12.74, 1.31)
5	16.75	0.80	1.9	(7.08, 2.37), (11.85, 1.41)
6[a]	-	-	-	-
7	22.3	1.08	8.5	(8.11, 2.75), (11.40, 1.96)
8	22.5	1.09	1.7	(8.99, 2.50)

[a] Unable to be measured due to Schottky-like behavior at low temperatures, likely due to carrier-depleted quantum wells.

our work here, aside from the discrete Fourier transform, come from samples not being perfect squares, contact asymmetry, and the square van der Pauw geometry used, which has been known to introduce some error into the measurements [16].

IV. CONCLUSION

We present results from the magnetotransport measurements and Shubnikov-de Haas oscillation analysis of several different AlGaAs/InAlGaAs multiple quantum well photocathode samples. We found that a cooler growth temperature of 505°C offered the best transport mobility and therefore demonstrated a higher material quality than the other samples studied, including those grown at 520°C and 535°C as well as those with modifications to the AlGaAs barrier and one with fewer quantum wells. We also found that effective masses were consistently higher than predicted for strained AlGaAs or InAlGaAs of the compositions we used, with the lowest m^* observed for the sample grown with a thicker AlGaAs barrier layer and the highest m^* observed for the sample grown with digital alloy AlGaAs layers. For many samples, we also found that effective mass increased with increasing applied magnetic field. Our analysis of the quantum and transport lifetimes suggests that large angle scattering, likely from ionized impurity atoms from modulation doping layers, dominates the scattering for all samples studied. Frequency analysis was performed on the SdH oscillations at 2 K for all samples, but poor resolution of the discrete Fourier transform due to the limited number of oscillations observed placed severe restrictions on the precision and reliability of values calculated, and more work will be needed if these values are of further interest.

From this work, we are able to better inform the growth and design conditions of future AlGaAs/InAlGaAs quantum well and 2DEG systems, specifically by employing slightly cooler growing temperatures. We especially hope to continue our work in optimizing and developing these systems as spim-polarized photocathodes to improve the performance and continued operation of particle accerlators' electron beam facilities as they seek to explore the structure and interactions of sub-atomic particles.

ACKNOWLEDGMENTS

I would like to thank Dr. Chris Palmstrøm for his guidance and insight throughout this project, as well as for welcoming me into his lab without any materials science background and challenging me to both engage deeply with the world of III-V growth and characterization as well as to remember that having fun is important too. Much of the success of this work I also owe to my graduate advisors Jason Dong and Aaron Engel for teaching me all of the theoretical foundations and lab skills that I used this summer, as well as spending many hours helping me with finicky soldering. To the entire Palmstrøm lab, I offer my gratitude for the welcoming and friendly environment you provided me with this summer. For making this entire opportunity not only possible but profoundly engaging and educational, I sincerely thank the UCSB Physics REU Site Director, Dr. Sathya Guruswamy. Funding for this work was provided through NSF REU Grant PHY-1852574.

[1] C. Hernandez-Garcia, P. G. O'Shea, and M. L. Stutzman, Physics Today **61**, 44 (2008), https://doi.org/10.1063/1.2883909.
[2] W. Liu, Y. Chen, W. Lu, A. Moy, M. Poelker, M. Stutzman, and S. Zhang, Applied Physics Letters **109**, 252104 (2016), https://doi.org/10.1063/1.4972180.
[3] J. Clendenin, in *Proceedings Particle Accelerator Conference*, Vol. 2 (1995) pp. 877–881 vol.2.
[4] P. S. Peercy and G. C. Osbourn, JOM **39**, 14 (1987).
[5] Y. A. Mamaev, L. G. Gerchikov, Y. P. Yashin, D. A. Vasiliev, V. V. Kuzmichev, V. M. Ustinov, A. E. Zhukov, V. S. Mikhrin, and A. P. Vasiliev, Applied Physics Letters **93**, 081114 (2008), https://doi.org/10.1063/1.2976437.
[6] L. J. van der Pauw, Philips Research Reports **13**, 1

(1958).
[7] M. Mashita, Y. Hiyama, K. Arai, B.-H. Koo, and T. Yao, Japanese Journal of Applied Physics **39**, 4435 (2000).
[8] P. Coleridge, in *Encyclopedia of Condensed Matter Physics*, edited by F. Bassani, G. L. Liedl, and P. Wyder (Elsevier, Oxford, 2005) pp. 248–256.
[9] L. Wang, M. Yin, A. Khan, S. Muhtadi, F. Asif, E. S. Choi, and T. Datta, Physical Review Applied **9**, 024006 (2018), arXiv:1707.07722 [cond-mat].
[10] M. Ben Shalom, A. Ron, A. Palevski, and Y. Dagan, Physical Review Letters **105**, 206401 (2010).
[11] H. Cao, J. Tian, I. Miotkowski, T. Shen, J. Hu, S. Qiao, and Y. P. Chen, Physical Review Letters **108**, 216803 (2012).
[12] J. Yuan, M. Hatefipour, B. A. Magill, W. Mayer, M. C. Dartiailh, K. Sardashti, K. S. Wickramasinghe, G. A. Khodaparast, Y. H. Matsuda, Y. Kohama, Z. Yang, S. Thapa, C. J. Stanton, and J. Shabani, Physical Review B **101**, 205310 (2020).
[13] I. Vurgaftman, J. R. Meyer, and L. R. Ram-Mohan, Journal of Applied Physics **89**, 5815 (2001).
[14] D. G. Hayes, C. P. Allford, G. V. Smith, C. McIndo, L. A. Hanks, A. M. Gilbertson, L. F. Cohen, S. Zhang, E. M. Clarke, and P. D. Buckle, Semiconductor Science and Technology **32**, 085002 (2017).
[15] P. T. Coleridge, Physical Review B **44**, 3793 (1991).
[16] A. Ramadan, R. Gould, and A. Ashour, Thin Solid Films **239**, 272 (1994).